ACS APPLIED MATERIALS & INTERFACES

www.acsami.org

Research Article

Hydrogel-Gated MXene-Graphene Field-Effect Transistor for Selective Detection and Screening of SARS-CoV-2 and *E. coli* Bacteria

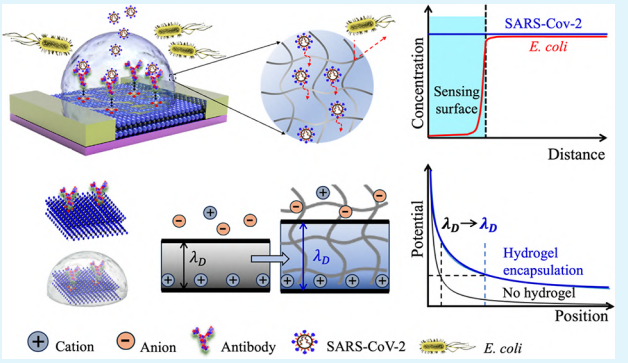
Jiaoli Li, Jiabin Liu, Congjie Wei, Xinyue Liu, Shaoting Lin, and Chenglin Wu*

Cite This: *ACS Appl. Mater. Interfaces* 2025, 17, 2871−2883

Read Online

ACCESS | Metrics & More | Article Recommendations | Supporting Information

ABSTRACT: Field-effect transistor (FET) biosensors have significantly attracted interest across various disciplines because of their high sensitivity, time-saving, and label-free characteristics. However, it remains a grand challenge to interface the FET biosensor with complex liquid media. Unlike standard liquid electrolytes containing purified protein content, directly exposing FET biosensors to complex biological fluids introduces significant sensing noise, which is caused by the abundance of nonspecific proteins, viruses, and bacteria that adsorb to the biosensor surfaces. In this work, we leverage the hydrogel encapsulation on an MXene−graphene-based FET, which selectively allows the permeation of viruses (e.g., SARS-CoV-2) and bacteria (e.g., *E. coli*), leading to the high-specificity detection of those biomarkers. The results demonstrated that hydrogel encapsulation could successfully detect the SARS-CoV-2 biomarker at 1 fg/mL while preventing the diffusion of *E. coli* biomarkers, and the obtained signal output amplitude is twice that of sensors without hydrogel encapsulation, demonstrating significant advantages over conventional bare sensors.



KEYWORDS: *field-effect-transistor (FET), hydrogel gating, selective transport/screening, SARS-CoV-2 virus, /iE. coli bacteria*

Downloaded via MICHIGAN STATE UNIV on March 23, 2025 at 20:37:42 (UTC).
See https://pubs.acs.org/sharingguidelines for options on how to legitimately share published articles.

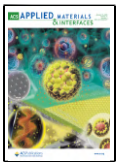
1. INTRODUCTION

Biosensors have gained much attention in biosensing technology for a wide range of bioanalyte detection and monitoring owing to their low costs, high flexibility, and designable sizes. Based on the sensing analytes, such as cancer diagnosis,[1] wound healing,[2] drug delivery,[3] and virus identification,[4,5] a large variety of sensor-related applications have emerged, such as photo-transistors,[6−8] piezoelectric sensors,[9] and FETs.[10,11] Among these technologies, FET sensors are a promising method for precisely detecting biomarkers.

Typically, a FET sensor is a type of transistor in which the electrical conductivity between two electrodes, known as the source and drain, is modulated by a third gate terminal through an insulator.[12] The threshold voltage variations caused by the absorption of the biomolecules to the sensing surface are regarded as the signal output of biomarker detection. In contrast, the charge biomolecule addition is equivalent to an extra voltage from the gate terminal. Nanomaterials, such as graphene,[13−15] silicon nanowires,[16] $MoSe_2$,[17] 2D carbides,[11−20] and carbon nanotube[21] have been widely applied in FET sensors to work as sensing materials. Specific biological probes, such as nucleic acids, antibodies, enzymes, and aptamers, are functionalized on the sensing surface to capture the corresponding biomarkers. We can determine the types and concentrations of target biomarkers by analyzing the signal output resulting from the biomarkers captured from the environment. The FET sensor's ability to detect in real time and its label-free analysis makes it superior to other biosensors. However, the development of FET sensors is severely hampered by their exposed sensing surface and liquid-based electrolytes, which can raise problems when applied to complex environments, such as *in vivo* detection. Specifically, the exposed sensing surface destabilizes its presence in the body and leads to increased absorption of nonspecific biomarkers, resulting in false signal transduction in FETs.[22] On the other hand, while it is essential to operate FETs, the commonly used liquid electrolyte can lead to sensor degradation as the liquid environment accelerates the breakdown of many sensing materials,[23] which is detrimental to their long-term effectiveness as well as the duration of the biosensors.

Due to these disadvantages, the liquid electrolytes in the traditional transistor with the gel membrane are vastly replaced by gel-gated transistors, which have aroused increasing research

Received: July 20, 2024
Revised: December 20, 2024
Accepted: December 25, 2024
Published: January 7, 2025



© 2025 American Chemical Society

https://doi.org/10.1021/acsami.4c12130
ACS Appl. Mater. Interfaces 2025, 17, 2871−2883

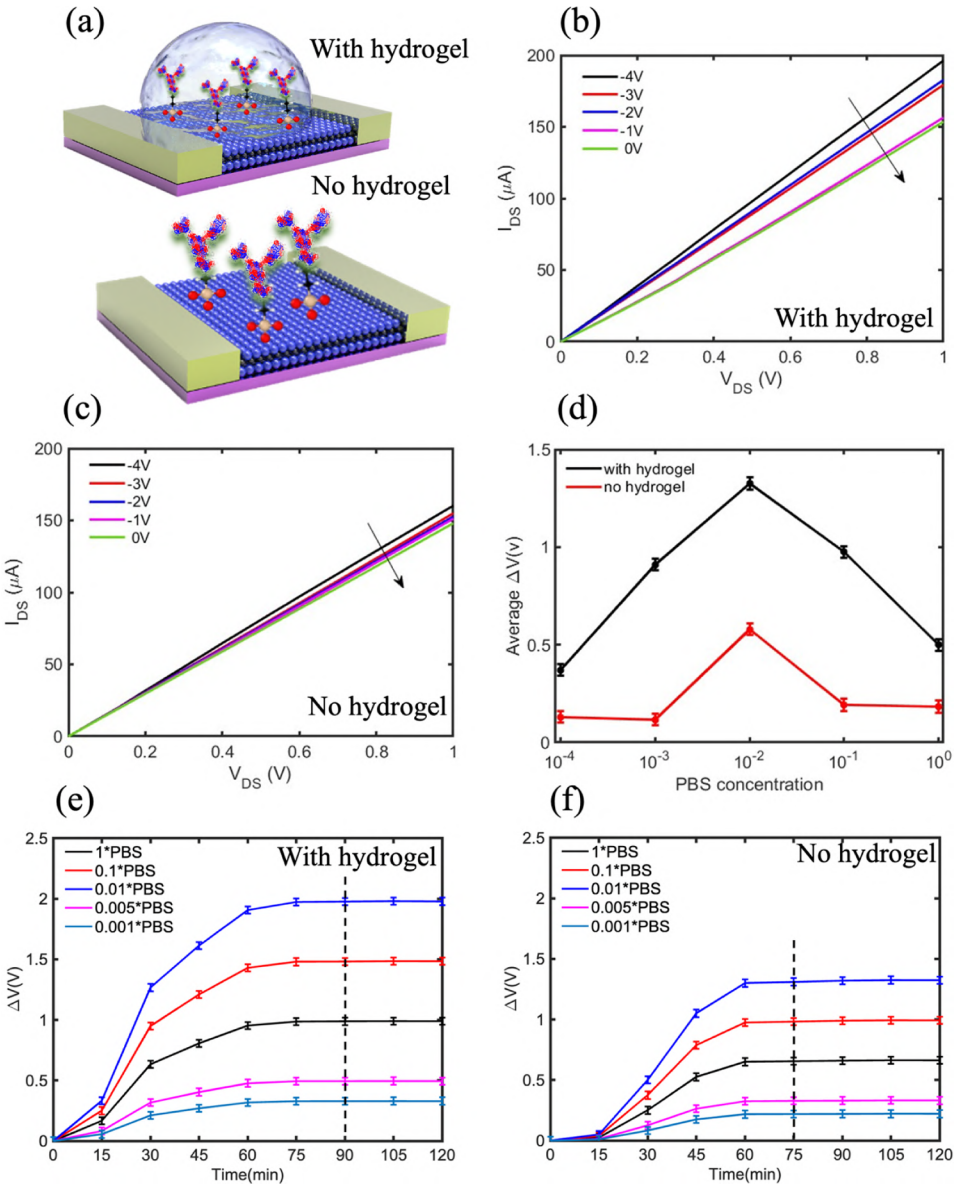


Figure 1. Hydrogel effects illustration: (a) schematic of the sensor with and without hydrogel encapsulation; Ohmic contact information on sensor (b) with and (c) without hydrogel encapsulation; (d) PBS concentration versus average Dirac point shifting. PBS concentration effects on the sensor and the stable time (e) with and (f) without hydrogel encapsulation.

enthusiasm.[24] Gel-gating can improve the shortcomings of exposed sensing surfaces in traditional FET sensors and could also lead to potential sensitivity enhancement due to surface modification. Unlike traditional sensors, the FET sensors with hydrogel encapsulation require biomarkers to diffuse through the polymer networks of the hydrogel before reaching the sensing surface. The hydrogel encapsulation not only creates an enclosed environment for the sensing material but also introduces a new design space to selectively pass specific biomarkers by designing the polymer network of the hydrogel. Dumitru et al.[25] adopted a jellified alginate-based capsule to gate an organic transistor and reduce the operation gate voltage. Bay et al.[22] encapsulated multiple specific receptors independently into the hydrogel gate to improve biosignal transduction at the molecular level. Inspired by these explorations, gel-gated FET sensors present a method to enhance their performance and enrich the detection environment due to selective diffusion effects, representing a significant breakthrough for further development. However, the gel matrix in current gel-gated FET sensors might allow nonspecific binding of biomolecules, leading to false positives or reduced sensitivity.

In this paper, the sensing surface of the MXene−graphene-based FET biosensor was encapsulated by a mesh-sized-designed hydrogel membrane for the ultrasensitive detection of the SARS-CoV-2 virus and *E. coli* bacteria. The specific antibodies of SARS-CoV-2 and *E. coli* were immobilized on the MXene−graphene-based sensing surface via APTES to work as the bioreceptor and capture the corresponding biomarkers to realize specific detection. From our previous research,[26] the addition of MXene not only improves signal output through capacitance and bandgap modulation but also enhances the sensor's ability to immobilize diverse bioprobes due to the abundance of functional groups on the MXene surface. Specially designed hydrogel encapsulation not only enhances accuracy through size-dependent filtration but also reduces effective solute diffusivity and obstructs the penetration of the sensing

https://doi.org/10.1021/acsami.4c12130
ACS Appl. Mater. Interfaces 2025, 17, 2871−2883

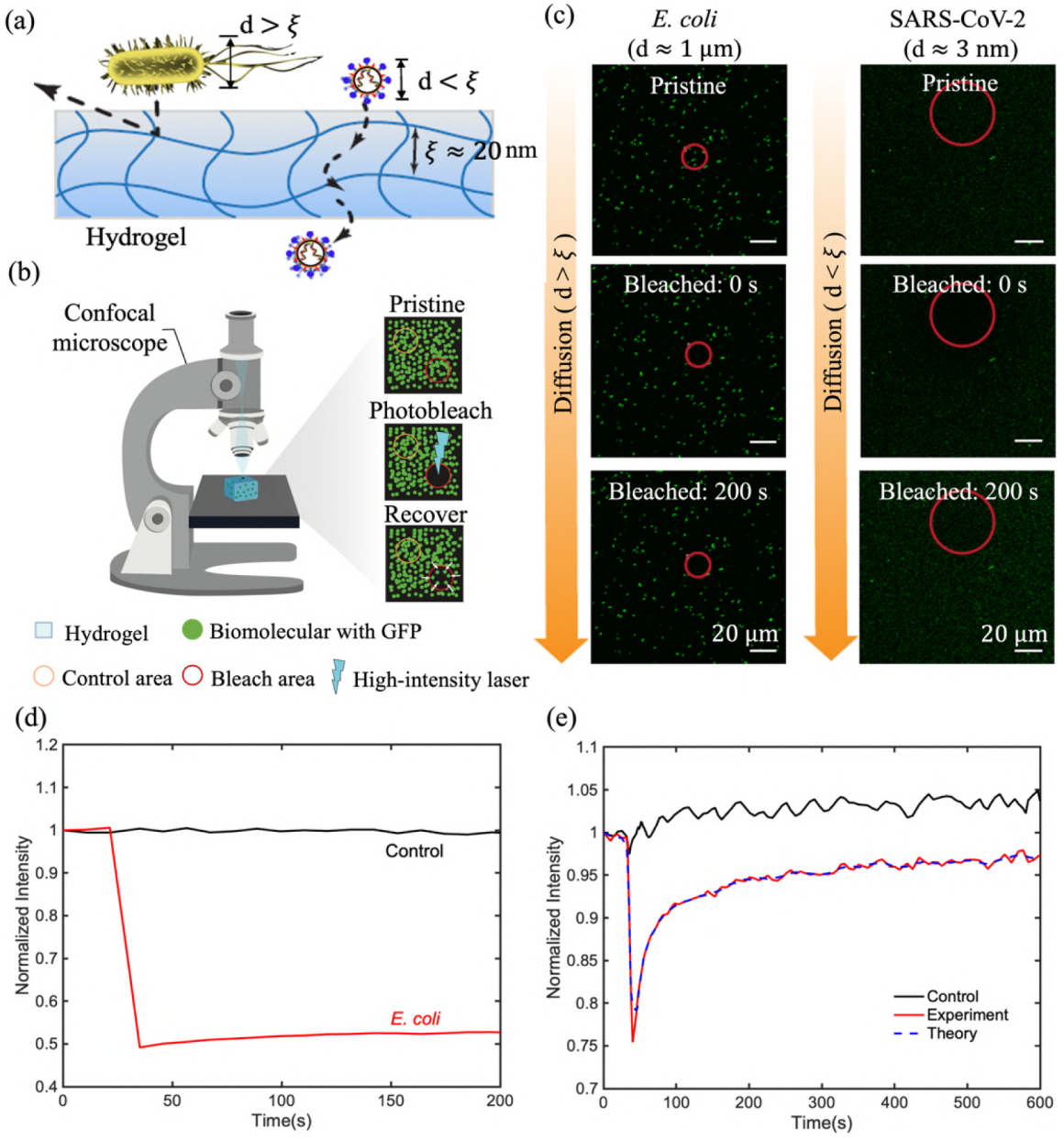


Figure 2. Transport characterizations of *E. coli*-GFP and fluorescence-labeled SARS-CoV-2 in hydrogels. (a) Schematic illustration of the selective transport of *E. coli*-GFP and fluorescence-labeled SARS-CoV-2 in hydrogels based on their size differences. (b) Schematic illustration of the experimental setup for the FRAP experiment. (c) Representative confocal image sequences of *E. coli*-GFP and fluorescence-labeled SARS-CoV-2 from FRAP experiments. The intensity of *E. coli*-GFP remains unchanged after bleaching, whereas the intensity of fluorescence-labeled SARS-CoV-2 gradually recovers after bleaching. (d) Plot of the normalized intensity versus time for the bleached and control regions of *E. coli*-GFP. (e) Plot of the normalized intensity versus time for the bleached and control regions of fluorescence-labeled SARS-CoV-2. The dotted line represents the fitting curve for extracting the diffusivity.

material. Results indicate that hydrogel encapsulation, functioning as a gel-based gate, controls biomarker access to the sensing surface and amplifies the signal output. Our research demonstrates the potential for deploying our sensor in complex environments. It opens the door to creating multifunctional *in vivo* sensors capable of analyte detection, potentially transforming disease diagnosis methods.

2. RESULTS AND DISCUSSION

2.1. Diffusion Effect on Gating. *2.1.1. Ohmic Contact.* To investigate the connection quality between the sensing film and electrodes, a voltage gradient ranging from −4 to 0 V was applied to both the HE sensor and the bare sensor (Figure 1a). The linear current−voltage (I_D−V_{DS}) curves shown in Figure 1b,c confirm the Ohmic contact behavior of the metal electrodes with the graphene−MXene-based semiconductor. The results indicate a good connection, with the HE-sensor demonstrating lower contact resistivity (5 kΩ) compared to the bare sensor (6.25 kΩ), as calculated from the average slope of the I_D−V_{DS} curves at various V_{DS} values.

2.1.2. PBS Concentration Effects. Phosphate Buffered Saline (PBS), a water-based salt solution, was used as the electrolyte in the FET sensor to explore its impact on the baseline signal and biomarker detection. Five PBS concentrations (0.001× PBS,

https://doi.org/10.1021/acsami.4c12130
ACS Appl. Mater. Interfaces 2025, 17, 2871−2883

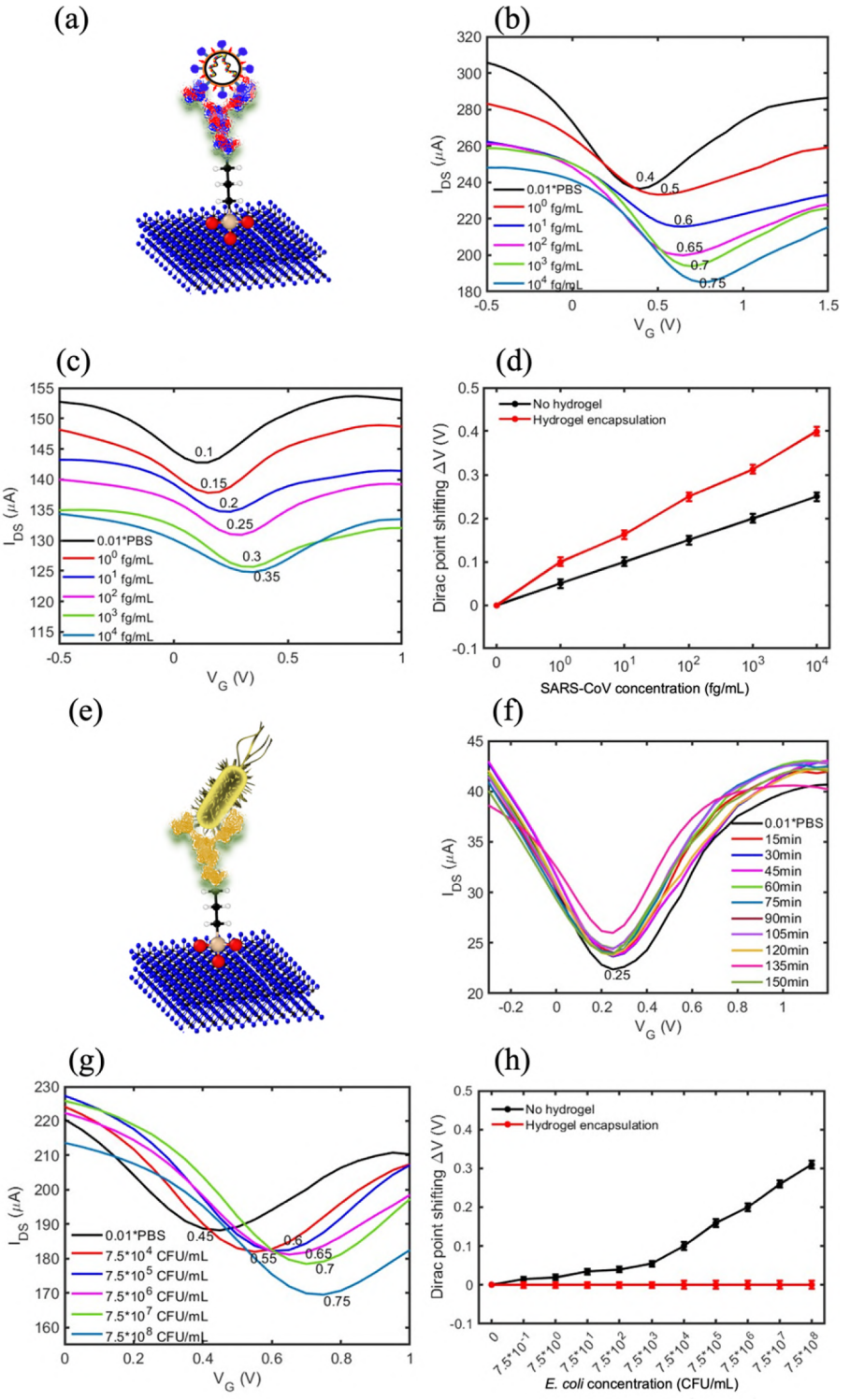


Figure 3. Sensor validation: (a) schematic of SARS-CoV-2 antibody-based sensor; (b)−(c) I_{DS}−V_G curve of the SARS-CoV-2 antibody-based sensor with and without hydrogel encapsulation. (d) Average gate voltage shifting ΔV (average $(V_G - V_0)$) versus concentration of SARS-CoV-2; (e) schematic of the *E. coli* antibody-based sensor; (f)−(g) I_{DS}−V_G curve of the *E. coli* antibody-based sensor with and without hydrogel encapsulation. (h) Average gate voltage shifting ΔV (average $(V_G - V_0)$) versus concentration of *E. coli* sensor with and without hydrogel encapsulation.

0.005× PBS, 0.01× PBS, 0.1× PBS, and 1× PBS) were tested for both HE sensors and bare sensors to determine the optimal concentration.

By comparing the Dirac point shifting amplitudes under different PBS concentrations, we observed that both sensors exhibited maximum Dirac point shifting at 0.01× PBS (Figure 1d). This behavior is attributed to the interplay between the Debye length and electrostatic screening effects. At low PBS concentrations (10^{-4} to 10^{-2}), the extended Debye length allows for stronger electrostatic interactions between the sensor and charged species over a larger distance, enhancing both baseline signal output and biomarker detection. Increasing the

https://doi.org/10.1021/acsami.4c12130
ACS Appl. Mater. Interfaces 2025, 17, 2871−2883

ionic concentration within this range amplifies these interactions, resulting in larger Dirac point shifts. Beyond 10^{-2} PBS, higher PBS concentrations shorten the Debye length, leading to stronger electrostatic screening that reduces the sensor's effective interaction range. This results in smaller Dirac point shifts as both the baseline signal and biomarker detection diminish.

PBS concentration, as an electrolyte, similarly affects both baseline signal and biomarker detection by modulating Debye length and electrostatic screening. The nonlinear relationship between PBS concentration and Dirac point shifting highlights the importance of optimizing PBS concentration to balance baseline signal strength and biomarker detection. Based on these findings, 0.01× PBS was selected as the optimal concentration, achieving the best balance between signal strength and detection performance. Besides, the HE sensor exhibited more significant Dirac point shifting than the bare sensor due to the hydrogel's porous structure, which likely slows ion mobility near the sensor. This reduced mobility decreases the screening effect of ions, enhancing the signal output at both low and high ionic concentrations.

Additionally, as shown in Figure 1e,f, the Dirac point of the HE sensor stabilized at 90 min, compared to 75 min for the bare sensor. Both sensors exhibited time-dependent Dirac point shifting behavior, with the difference in stabilization time attributed to the diffusion process of PBS through the hydrogel encapsulation layer in the HE sensor. When charged biomarkers dissolved in 0.01× PBS reach the sensor surface, they interact with the probe, triggering charge redistribution and gradual adjustments in the electrostatic environment. These changes take time to stabilize as the system moves toward equilibrium, resulting in a steady signal output. The longer stabilization time observed in the HE sensor reflects the additional diffusion step imposed by the hydrogel layer, which slows the transport of PBS and biomarkers to the sensing surface. To ensure consistent results, these stabilization times (90 min for the HE sensor and 75 min for the bare sensor) were used as the standard for PBS electrolyte treatment throughout the experiments.

Overall, the experiments confirmed that the PBS concentration significantly affects sensor performance by modulating Debye length and electrostatic screening effects. Both HE sensors and bare sensors achieved maximum Dirac point shifting at 0.01× PBS, demonstrating that this concentration optimizes baseline signal strength and biomarker detection. Additionally, the hydrogel layer in HE sensors not only enhanced signal output but also extended stabilization time due to its diffusion effects, offering a unique advantage for controlled and sensitive detection.

2.2. Selective Transport Experiment Verification. To characterize the selective transport through hydrogels based on the size of biomolecules, we performed fluorescence recovery after photobleaching (FRAP) experiments on the PAAm hydrogel mixed with *E. coli*-GFP and fluorescence-labeled SARS-CoV-2, respectively (Figure 2a). FRAP is a microscopic technique used to measure the diffusivity of fluorescent molecules in cells or tissues. It utilizes a high-intensity laser to photobleach the fluorescent molecules in a targeted area and subsequently records the intensity of the bleached area continuously (Figure 2b). Confocal images and fluorescence intensity $I(t)$ were collected every 10 s postbleaching and normalized to the initial intensity I_0 before bleaching. The resulting full bleaching confocal images and normalized fluorescence intensity curves over time are shown in Figure 2c,e.

As shown in Figure 2c, the size of *E. coli*-GFP is around 1 μm, while the size of fluorescence-labeled SARS-CoV-2 is estimated to be 3.4 nm using the equation $R=0.066M^{1/3}$,[27] where M represents the molecular mass of fluorescence-labeled SARS-CoV-2. The intensity curve of *E. coli*-GFP remained unchanged after photobleaching, whereas the fluorescence intensity of labeled SARS-CoV-2 recovered fully within 2 min (see the supplementary video), indicating its ability to diffuse through the hydrogel.

To identify the diffusivity from the measured normalized intensity as a function of time, we adopted the Soumpasis equation[28]

$$\frac{I(t)}{I_0} = e^{-\omega^2/2Dt}\left(B_0\left(\frac{\omega^2}{2Dt}\right) + B_1\left(\frac{\omega^2}{2Dt}\right)\right) \quad (1)$$

where $I(t)/I_0$ is the normalized fluorescence intensity, ω is the radius of the bleached spot, t is the time, D is the diffusion coefficient, B_0 and B_1 are the modified Bessel functions of the first kind of order 0 and 1, respectively. Using this equation, the diffusion coefficients of *E. coli*-GFP and fluorescence-labeled SARS-CoV-2 in PAAm hydrogels were determined to be 0 and 3.75×10^{-12} m/s,[2] respectively.

These results demonstrate that the size of the biomolecules determines their ability to penetrate the hydrogel. The *E. coli*-GFP (~1 μm) could not diffuse through the hydrogel due to its size being significantly larger than the hydrogel mesh size (~20 nm). In contrast, fluorescence-labeled SARS-CoV-2 (~3.4 nm) was able to diffuse freely through the hydrogel, as its size is much smaller than the mesh size. This experiment confirms that the PAAm hydrogel serves as an effective intermediate layer for the selective transport of biomolecules based on size. While using the SARS-CoV-2 protein rather than the actual virus introduces some limitations in fully demonstrating the sensor's detection capability, this approach allowed us to establish a size-based biomarker control to highlight the hydrogel's role in selective transport. This proof-of-concept study demonstrates the feasibility of hydrogel-controlled selective transport for similar applications.

2.3. Specific Detection Experiment. To investigate the effects of biomarker concentration on the sensing signal outputs, experiments were conducted using both HE sensors and bare sensors for SARS-CoV-2 protein and *E. coli* detection.

2.3.1. SARS-CoV-2 Detection. The SARS-CoV-2 antibody was immobilized on the sensing surface to capture the protein (Figure 3a). Five concentrations of the protein (1 fg/mL, 10 fg/mL, 10^2 fg/mL, 10^3 fg/mL, and 10^4 fg/mL) were tested. The $I_{DS}-V_G$ curves of HE and the bare sensors are shown in Figure 3b,c. In HE sensors, the hydrogel encapsulation delays the diffusion of biomarkers to the sensing surface. Signal outputs were recorded every 15 min for 2.5 h until stabilization, as shown in Figure S1a. For the lowest concentration (1 fg/mL), the signal stabilized after 120 min, indicating complete biomarker diffusion and saturated antibody−protein bonding. In contrast, for the highest concentration (10^4 fg/mL, shown in Figure S1b), stabilization occurred faster, within 90 min.

We observed that the addition of protein leads to the sensors' Dirac point continuously shifting to the right due to the charge transfer to the antibody probes. Since the target protein is negatively charged, its capture increases the overall negative charge in the electrolyte. This results in a rightward shift of the Dirac point due to the p-doping effect. Higher protein concentrations caused greater shifts in the Dirac point, as

https://doi.org/10.1021/acsami.4c12130
ACS Appl. Mater. Interfaces 2025, 17, 2871−2883

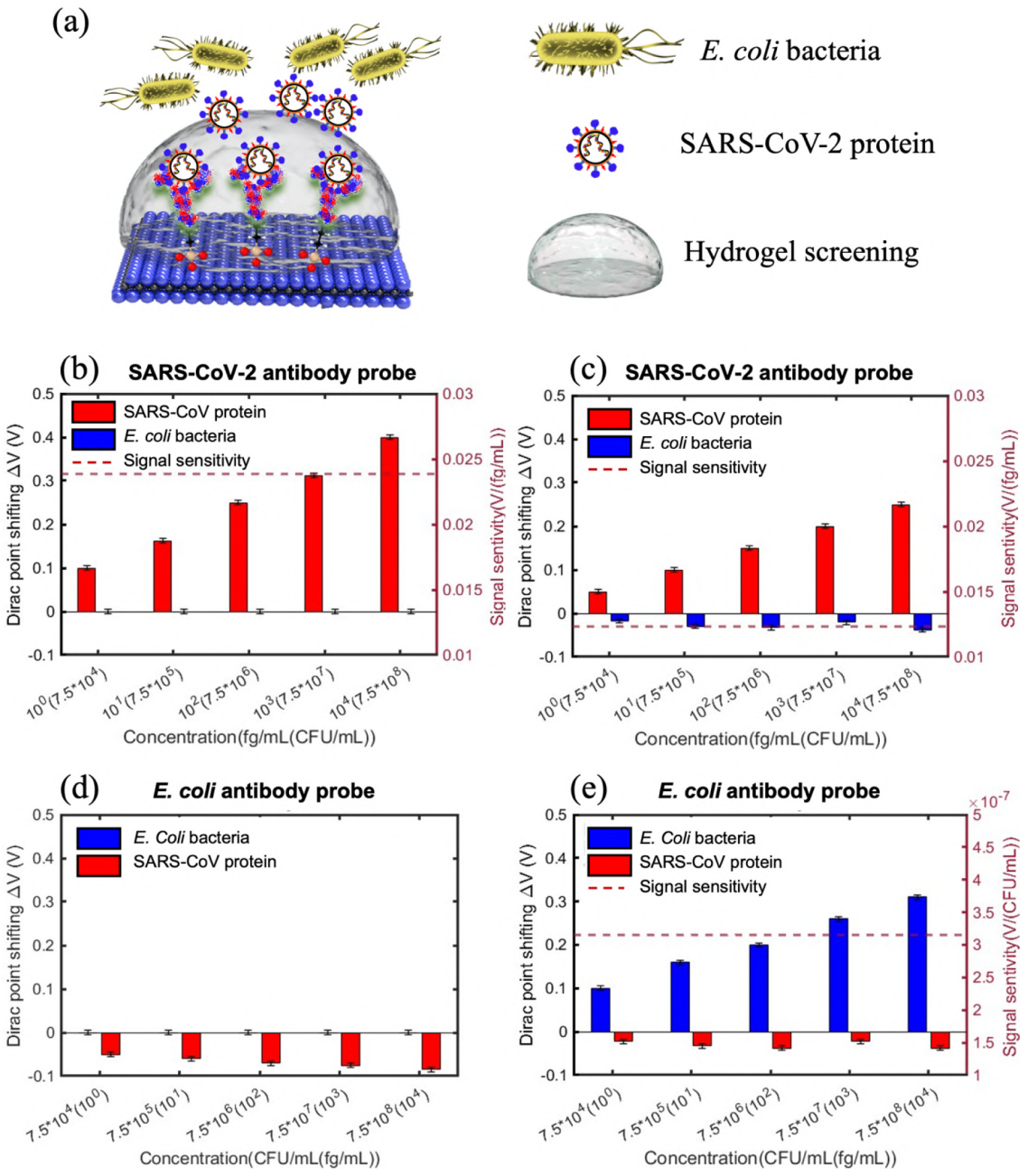


Figure 4. Specific detection: (a) schematic of the hydrogel screening effect and (b)−(c) detection results of HE sensors and bare sensors based on the SARS-CoV-2 antibody probe; (d)−(e) detection results of HE sensors and bare sensors based on the *E. coli* antibody probe.

illustrated in Figure 3d. The Dirac point shifts were approximately twice as large for HE sensors compared with bare sensors, demonstrating the signal enhancement effect of hydrogel encapsulation.

2.3.1.1. E. coli Detection. The *E. coli* K12 antibody was immobilized on the sensing surface (Figure 3e), and five different concentrations of *E. coli* bacteria (7.5×10^4 CFU/mL, 7.5×10^5 CFU/mL, 7.5×10^6 CFU/mL, 7.5×10^7 CFU/mL, and 7.5×10^8 CFU/mL) were tested. The results for HE sensors and bare sensors differed significantly due to the size of the *E. coli* bacteria (approximately 2.0 μm long and 0.25−1.0 μm in diameter), which is larger than the mesh size of the hydrogel.

For HE sensors, the hydrogel encapsulation effectively blocked the *E. coli* bacteria, preventing them from diffusing to the sensing surface. This resulted in no Dirac point shifting during the 150-min observation period (Figure 3f). The absence of Dirac point shifts indicates that the hydrogel successfully screened out the *E. coli*, leaving the sensor unchanged. In contrast, bare sensors showed continuous rightward Dirac point shifts with increasing *E. coli* concentrations (Figure 3g). The $I_{DS}-V_G$ curves for bare sensors revealed consistent ionic behavior at the sensing surface, indicating that *E. coli* bacteria were successfully captured by the antibodies.

The initial currents in $I_{DS}-V_G$ curves for HE and bare sensors at different times were plotted in Figure S1c. While the currents in HE sensors remained largely unchanged, the currents in bare sensors gradually decreased over time. The average Dirac point shifts ($\Delta V = V_G - V_0$) versus *E. coli* concentration are summarized in Figure 3h. HE sensors showed no Dirac point shifting due to the hydrogel's screening effect, while bare sensors

https://doi.org/10.1021/acsami.4c12130
ACS Appl. Mater. Interfaces 2025, 17, 2871−2883

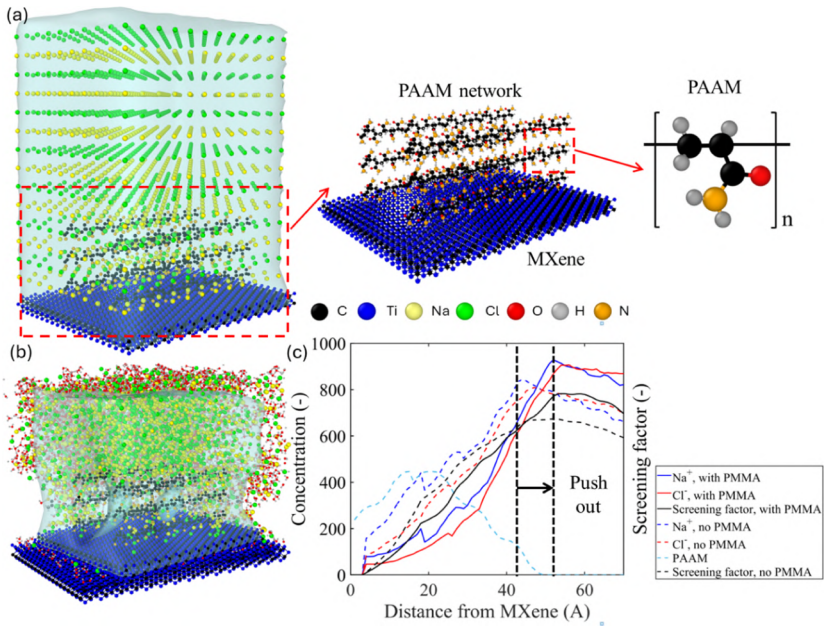


Figure 5. (a) Modeling setup for the first step of the MXene−PAAM−NaCl solution system. (b) Snapshot after stabilization. (c) Concentration distribution and screening factor comparison.

displayed a quasi-bilinear relationship between Dirac point shifts and *E. coli* concentration. This relationship allows the concentration of *E. coli* in the environment to be inferred from the bare sensor's signal output.

Overall, these experiments validated the ability of our sensors to detect biomarkers with high specificity. For SARS-CoV-2 detection, hydrogel encapsulation enhanced the signal by amplifying the Dirac point shift and improving the sensitivity. For *E. coli* detection, the hydrogel acted as an effective barrier, selectively preventing large-sized bacteria from reaching the sensing surface. Bare sensors, on the other hand, successfully captured *E. coli* and demonstrated a clear concentration-dependent response.

2.4. Specific Detection Results. Based on the specific affinity between an antibody and its corresponding biomarker, our sensors are designed to produce no significant signal when encountering mismatched biomarkers. This principle underpins their potential for targeted environmental detection. To evaluate the specific detection performance, we conducted experiments using SARS-CoV-2 antibody-based HE sensors and bare sensors to detect *E. coli* bacteria. Similarly, we used *E. coli* K12 antibody-based sensors to detect the SARS-CoV-2 protein. The hydrogel encapsulation was designed to act as a screening layer, filtering out *E. coli* bacteria, as illustrated in Figure 4a. The signal versus concentration results are presented in Figure 4b,e.

When using SARS-CoV-2 antibody-based HE sensors to detect *E. coli* bacteria, the hydrogel screening prevented any Dirac point shift, as shown in Figure 4b. However, for the corresponding bare sensor without hydrogel filtration (Figure 4c), Dirac point shifts were observed at increasing *E. coli* concentrations. These signals were weak and followed an irregular trend due to the mismatch between the SARS-CoV-2 antibody and *E. coli* biomarker, highlighting the specificity of the sensor compared to results obtained when detecting SARS-CoV-2 proteins.

In the reverse scenario, we applied *E. coli* antibody-based sensors to detect SARS-CoV-2 proteins. Here, Dirac point shifts were observed in both the HE and bare sensors. This is because SARS-CoV-2 proteins, being much smaller in size, diffused through the hydrogel encapsulation to reach the sensing surface. As shown in Figure 4d,e, the relationship between SARS-CoV-2 protein concentration and signal output was irregular due to the mismatch between *E. coli* antibodies and SARS-CoV-2 proteins. However, chemical bonding between antibodies and proteins was still formed, leading to Dirac point shifts. Notably, the hydrogel encapsulation enhanced signal output, with the HE sensor producing signal intensities that are approximately twice those of the bare sensor. Despite this, the Dirac point shifts were less pronounced than those observed when detecting *E. coli* bacteria.

Overall, these experiments confirmed the capability of our sensors for targeted detection. The specific interaction between antibodies and biomarkers enables the accurate identification of particular biomarkers. Furthermore, the hydrogel encapsulation not only filters out impurities via its tailored mesh size but also enhances signal output due to its low conductivity.

3. INVESTIGATION OF DEBYE LENGTH BY MOLECULAR DYNAMIC MODELING

To study the influence of the introduced polymer on the electric fields, we conducted molecular dynamics (MD) modeling cases using the Large-scale Atomic/Molecular Massively Parallel Simulator (LAMMPS) package. The PAAM polymer is chosen, and a network of PAAM is located on the surface of Ti_3C_2 MXene and soaked within the water with Na^+ and Cl^- ions, as shown in Figure 5. Initially, the H_2O molecules as well as Na^+ and Cl^- ions are uniformly arranged. Periodic boundary conditions are used in all directions. The size of the cell matches that of MXene along the in-plane directions, while a large interspace is set to create a vacuum and eliminate the influences from neighboring cells for the out-of-plane direction. ReaxFF potentials are used to define the interactions among all the elements included in the MXene, PAAM, and NaCl solution.

While modeling, the PAAM network is first stabilized with the NVT ensemble for 1 ns at room temperature before being constructed with MXene and NaCl solution. The whole system

https://doi.org/10.1021/acsami.4c12130
ACS Appl. Mater. Interfaces 2025, 17, 2871−2883

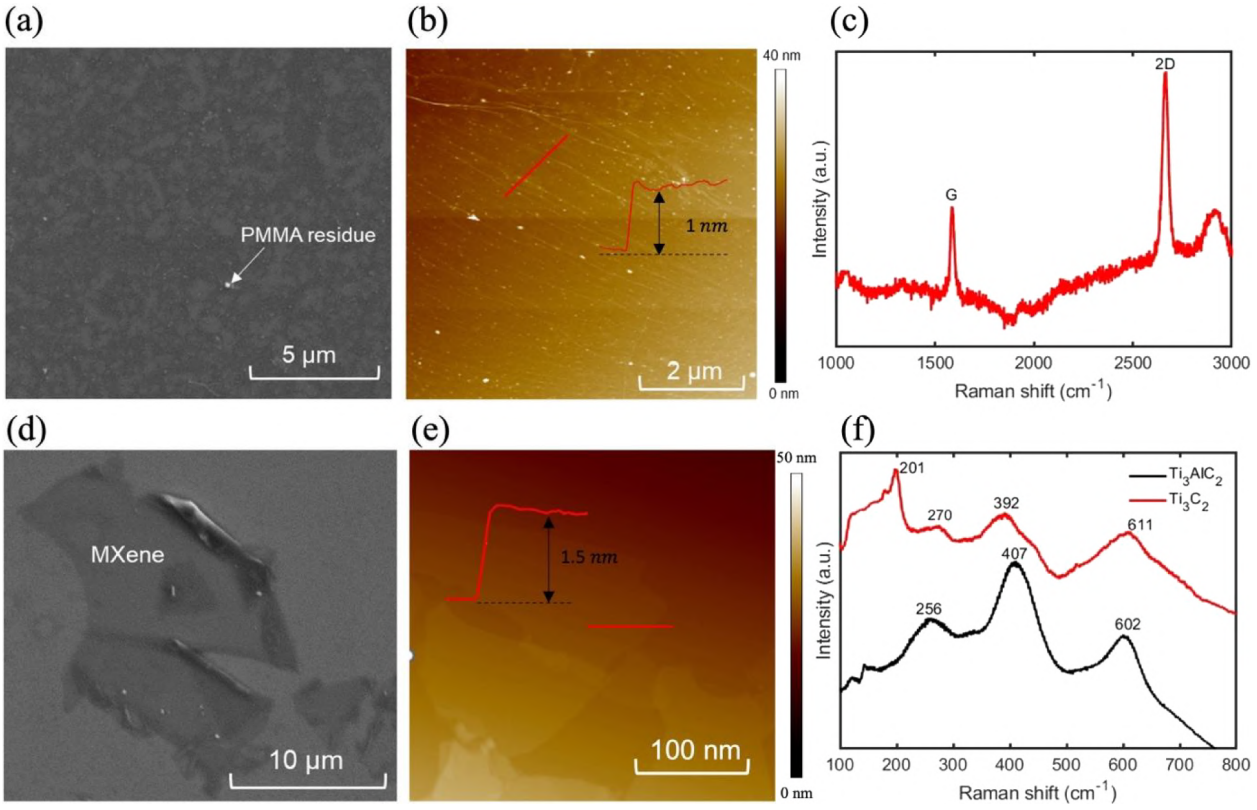


Figure 6. Graphene characterization: (a) SEM image, (b) AFM image, and (c) Raman spectrum of graphene; MXene characterization: (d) SEM image, (e) AFM image, and (f) Raman spectrum of MXene.

is then stabilized with an NVT ensemble for 2 ns at a relatively low temperature of 1 K to prevent the system from blowing up. Starting from this step, the PAAM network and MXene layer are thoroughly fixed with respect to displacement along all directions, while the NaCl solution can evolve freely. The diffusion process of Na^+ and Cl^- ions is then modeled with another NVT ensemble at 300 K for a total of 10 ns to reach equilibrium, as shown in Figure 5b. The water molecules reach a natural density in this process. The distribution of Na^+ and Cl^- ions is then extracted and used for screening factor calculations, which are shown in Figure 5c. To better illustrate the influence of the polymer, a benchmark case with only MXene and NaCl solution (no PMMA) is also modeled using the same setups and analyzed.

The influence of PAAM on the electric field on the surface of MXene is then analyzed by extracting the Na^+ and Cl^- ion distributions from the stabilized MXene−PAAM−NaCl solution system. The concentrations of Na^+ and Cl^- ions with respect to the distance from Ti_3C_2 MXene surface are extracted and used to calculate the screening factor using the following equation,

$$\text{Screening Factor} = \frac{\int_0^Z F([Na^+] - [Cl^-])}{|\sigma|} \quad (2)$$

Where F is the Faraday constant, Z is the distance from the Ti_3C_2 MXene surface, and σ is the MXene surface charge density.

The results (Figure 5c) show that compared with the benchmark case without any PAAM, the introduction of the PAAM network significantly pushed out the screening factor (i.e., Debye length). In both scenarios, the screening factor exhibits a two-phase pattern. However, in the PAAM network case, the transition from a rising trend to a plateau occurred later than in the benchmark case. This transition also coincided with the point at which the PAAM network ceased to exist. The estimated Debye length with the PAAM−MXene system is about 53 Å , increased by approximately 25% from the original 42 Å of the MXene alone.

4. MATERIAL CHARACTERIZATION AND SENSOR FABRICATION

4.1. Material Preparation. *4.1.1. Graphene.* The monolayer graphene is grown on the copper foil substrate via the chemical vapor deposition (CVD) method, with copper adopted as the catalyst substrate due to its low solubility of C atoms. In the synthesis process, a mixture of methane and hydrogen was applied to the copper for 10 min at a temperature of 1050 °C. The copper substrate was removed by using the wet transfer method to obtain the synthesized monolayer graphene. Subsequently, the graphene surface was coated with 2% poly(methyl methacrylate) (PMMA) and dried at 130 °C for 3 min. The PMMA−graphene−copper sandwich composite was then transferred to a copper etchant to remove the copper substrate, followed by five DI water rinses to eliminate any residual copper and etchant. The cleaned PMMA−graphene composite was transferred to a glass substrate and treated with acetone, isopropyl alcohol (IPA), and DI water to remove the PMMA.

4.1.2. MXene. A 0.5 g portion of Ti_3AlC_2 MAX phase (purchased from 11 Technology Co., LTD) powder was added gradually to the etchant (consisting of 10 mL of 9 mol HCl and 0.8 g of LiF). The etching process was conducted at room temperature with continuous stirring for 30 h. Then, the mixture

https://doi.org/10.1021/acsami.4c12130
ACS Appl. Mater. Interfaces 2025, 17, 2871−2883

was washed five times using centrifugation at 3500 rpm for 6 min to remove the etchant solution. A 1.5 h ultrasonication was applied to the obtained sediment to delaminate the multilayer MXene.

4.1.3. Hydrogel. To synthesize the PAAm hydrogel,[29] the powders of acrylamide (M_W = 71 g/mol) were dissolved in deionized water, yielding a pregel solution with a fixed acrylamide concentration of 12 wt %. 110 μL of 0.1 M ammonium persulfate (APS) was added as the thermal initiator, 500 μL of 0.23 wt % N, N′-Methylenebis(acrylamide) (MBAA, M_w = 154 g/mol) as the cross-linker, and 20 μL of N,N,N′,N′-tetramethylethylenediamine (TEMED) as the cross-linking accelerator in 10 mL of the pregel solution. Thereafter, the solution was used to cover and cure the sensing surface at 50 °C for 20 min.

4.1.4. APTES, Antibody, and Biomarkers. (3-Aminopropyl) triethoxysilane (APTES) used in this work was purchased from Sigma-Aldrich (St. Louis, MO, USA). The SARS-CoV-2 spike antibody (catalog no. 40150-D001) and recombinant 2019-nCoV spike protein S1 (catalog no. 40591-V08H) were purchased from SinoBiological (Wayne, PA, USA). The *E. coli* K12 antibody was purchased from Fisher Scientific (Pittsburgh, PA, USA), and the corresponding *E. coli* bacteria were cultured in our biolab. The SARS-CoV-2 antibody and *E. coli* antibody were diluted to 100 μg/mL and 10 μg/mL, respectively. The SARS-CoV-2 protein was dissolved in 0.01× PBS to prepare different concentrations for detection. The plate counting method was used to determine the initial number of cultured *E. coli* bacteria, and then 0.01× PBS was used to prepare *E. coli* bacteria with different concentrations.

4.2. Material Characterization. Scanning electron microscopy (SEM) (Helios 600) coupled with atomic force microscopy (AFM) (ICON) was used to characterize the geometric shapes of the synthesized materials. X-ray diffraction (XRD) detection was performed to explore the material's lattice structure. X-ray photoelectron spectroscopy (XPS) was conducted to acquire information about surface chemistry, including chemical composition and elemental oxidation states. Raman spectra were obtained to learn about the molecule types through their vibrational modes.

4.2.1. Graphene. The SEM image in Figure 6a shows the surface morphology of the graphene and the successful synthesis of the large-area graphene and its transfer to the silicon surface with a negligible amount of PMMA. The folds and wrinkles on the graphene film were caused by the nonuniformity of the copper foil substrate. The PMMA residue was a byproduct of the wet transfer process. The topography of the graphene was investigated through AFM imaging and is shown in Figure 6b. It indicates that the height of the graphene on the silicon wafer is around 1 nm, consistent with previous research.[30] Both wrinkles and the PMMA residue could be observed, which matches the SEM observations. Raman spectroscopy, as shown in Figure 6c, indicates that the CVD-grown monolayer graphene is of high quality, displaying minimal D band activity centered at 1352 cm^{-1} in the spectra, which is characteristic of monolayer graphene. The G band, centered at 1580 cm^{-1}, arises from the E_{2g} mode at the Γ-point and is the dominant in-plane vibrational mode. This band results from the stretching of the C−C bond in graphitic materials and is typical of all sp^2 carbon systems.[31] The 2D band (centered at 2690 cm^{-1}) is a second-order overtone of an in-plane vibration. It exhibits a symmetric shape with a full width at half-maximum (HWHM) of approximately 33 cm^{-1}. Moreover, it features a D-band to G-band intensity ratio of ~0.5I_D/I_G, indicating that the synthesized monolayer graphene is of high quality.

4.2.2. MXene. The MXene flake shows a flake size of around 5 μm in the SEM image (Figure 6d) and a height of 1.37 nm in the AFM image (Figure 6e), validating that the monolayer MXene flake was successfully delaminated from the multilayer MXene. Figure 6f shows the Raman spectrum of the Ti_3C_2 MXene and its MAX phase. Compared to Ti_3C_2, the broadened Raman bands of Ti_3C_2 after chemical etching suggest that multiple surface functional groups coexist in the MXene nanosheets. Moreover, one can observe that four sharp peaks occur at 201, 270, 392, and 611 cm^{-1}, which are indicative of MXene. Like Ti_3AlC_2, the peaks at 201 cm^{-1} can be assigned to the Ti−C vibration (A1g symmetry) of the oxygen-terminated $Ti_3C_2O_2$, while the peaks at around 392 cm^{-1} conform to the E_g vibrations. The peak at 612 cm^{-1} comes mostly from E_g vibrations of the C atoms in OH-terminated Ti_3C_2.

Figure S2 shows the XRD patterns of Ti_3C_2 MXene and the corresponding MAX phases (Ti_3AlC_2). The XRD pattern of the Ti_3AlC_2 displays various peaks centered at 9.55°, 19.15°, 34.02°, 38.7°, and 41.7°, which correspond to the indices (002), (004), (101), (104), and (105), respectively.[32] For comparison, the (002) peak of Ti_3C_2 MXene tends to shift toward a smaller angle and be broadened owing to the selective etching of Al atoms from Ti_3AlC_2. The weakening peak at around 39° reveals the exhaustion of Ti_3AlC_2. In addition to verifying the etching process, the XRD spectrum can be used to determine the *d*-spacing of the MXene sheets. The (002) peak of the dried MXene powder is located at 7.4°, while the peak for the MAX phase is at 9.5°. Based on Bragg's law, the *d*-spacing is 11.93 Å for MXene and 9.3 Å for the MAX phase, which coincides closely with the calculated thickness of a monolayer MXene.

Figure S3 presents the survey spectrum and the high-resolution XPS spectrum of Ti 2p, O 1s, F 1s, and C 1s regions of the prepared MXene on the silicon surface. As shown in Figure S3a, the obvious peaks at binding energy values of 282.58, 456.08, 532.58, and 684.96 eV are assigned to C 1s, Ti 2p, O 1s, and F 1s, respectively. The high-resolution XPS spectrum of Ti 2p in Figure S3b can be deconvoluted into 4 peaks corresponding to the Ti−C bonding, Ti(II), Ti(III), and Ti(IV). It should be noted that Ti(II), Ti(III), and Ti(IV) are caused by the formation of TiO_xF_y and TiC_xO_y during the partial oxidation of MXene. The high-resolution spectrum in the O 1s region (shown in Figure S3c) confirms the formation of Ti oxide (TiO_2) and demonstrates the presence of OH/O_x groups bonding to the MXene surfaces. The F group introduced during the HF etching process can be found in the F 1s spectrum (Figure S3d) as Ti−F and Al−F signals. Figure S3e shows the 2 chemical states of C: adsorbed C−Ti and C−C bonds. In summary, XPS analysis comprehensively clarified the surface chemical composition (Ti, O, F, and C) and functional groups (−F, −OH, and $-O_x$), and further clarified the Al-etching process and partial oxidation of the prepared MXene.[33]

4.2.3. Hydrogel. Figure S4 indicates a rough surface morphology for the hydrogel membrane. The distribution of component elements (C, N, and O) of the hydrogel was obtained by energy-dispersive X-ray spectroscopy (EDS). Figure S4b−d presents the distribution of these elements. All of these results show that the hydrogel adopted in this research is of good quality.

4.3. Electrochemical Characterization. The 3-electrode system was used to characterize the electrochemical properties of the sensing surface during the functionalization process. The

https://doi.org/10.1021/acsami.4c12130
ACS Appl. Mater. Interfaces 2025, 17, 2871−2883

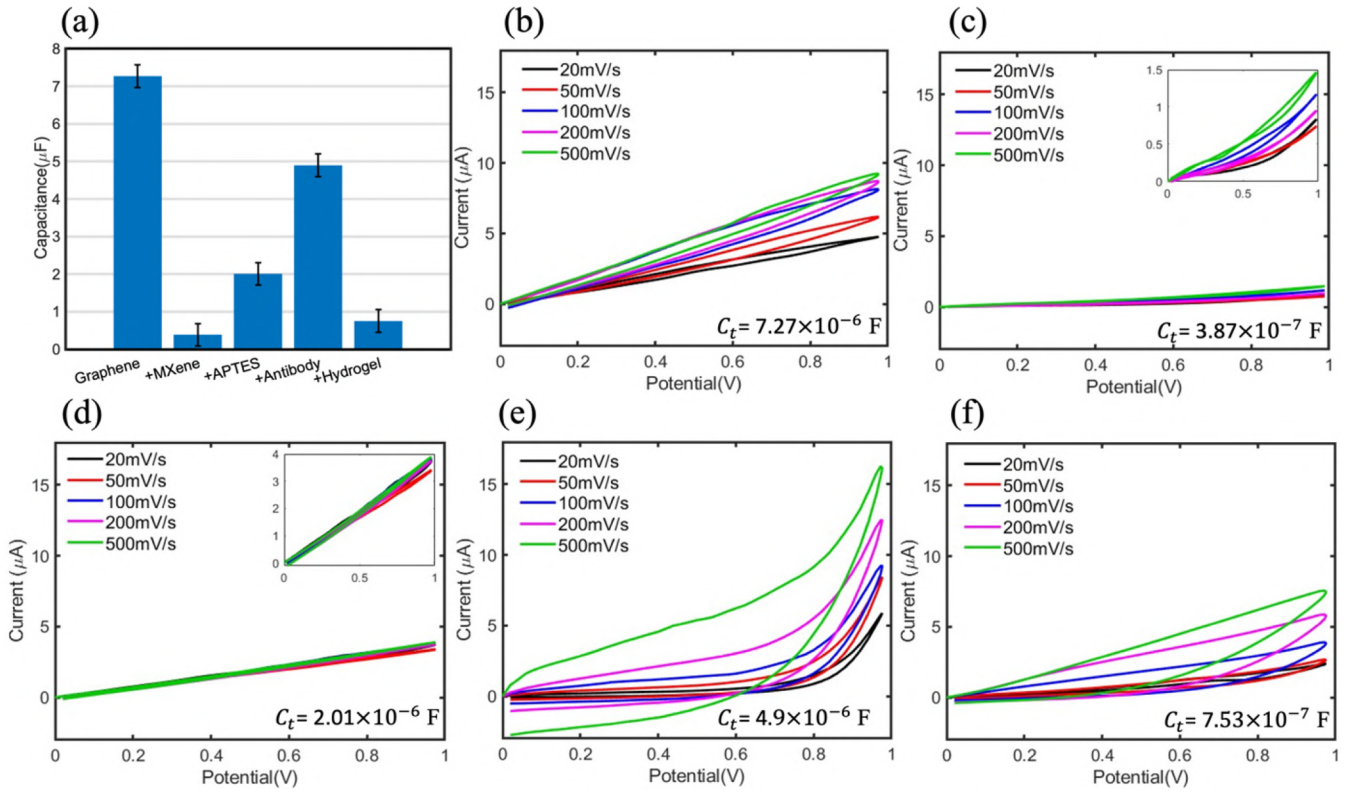


Figure 7. (a) Capacitance results summarization and separate cyclic voltammetry curve for (b) graphene, (c) graphene−MXene, (d) graphene−MXene−APTES, (e) graphene−MXene−APTES−antibody, and (f) graphene−MXene−APTES−antibody−hydrogel.

counter electrode was a platinum electrode, while the reference electrode was Ag/AgCl. The sensing surface obtained after different functionalization steps was used as the working electrode. The 0.01× PBS aqueous solution was used as the electrolyte to monitor the sensor's working condition.

Electrochemical properties of the sensing surface were studied in detail by performing cyclic symmetrical voltammetry (CV) curves on the sensing surface after every fabrication and functionalization process at varied scan rates (20, 50, 100, 200, and 500 mV/s). The window voltage was set from 0 to 1 V to avoid the presence of Faradaic current and obtain the capacitance of the sensing surface.[34] From the capacitance calculation results in Figure 7a, we know that the MXene coating could greatly decrease the capacitance (from 7.27 × 10^{-6} F to 3.87 × 10^{-7} F). During the functionalization process, the capacitance of the functionalized surface first decreased to 2.01 × 10^{-6} F after APTES treatment, then slightly increased to 4.9 × 10^{-6} F after antibody immobilization (Figure 7b,f). It should be noted that there was a decrease in the capacitance of the functionalized surface when it was encapsulated with the hydrogel membrane (7.53 × 10^{-7} F). This decreased capacitance contributes to signal enhancement regarding the sensor signal output.

Electrochemical impedance spectra (EIS) were conducted to acquire the electrochemical behavior of the sensing surface using the samples in the CV curve measurements. Nyquist plots in Figure S5 consist of a typical semicircle in the high-frequency region and a straight line in the low-frequency region, and the inset shows its equivalent circuit, where R_s, R_{ct}, C_{dl}, and Z_w represent the electrolyte resistance, charge-transfer resistance (R_{ct}) at the electrode/electrolyte surface, double-layer capacitance, and Warburg's impedance.[35] The diameter of the semicircle at a high frequency indicates internal resistance, which is related to R_{ct}. The small semicircle indicated favorable electrical conductivity, while the maximum value in the direction of the imaginary axis of the semicircle is related to the double-layer capacitance. Comparing the capacitance calculated for the Nyquist plot with that of the CV curves could verify the measurements. Based on the curve, we know that both the resistance and capacitance show a similar changing trend during the functionalization process. It is evident that the pure graphene electrode exhibits the highest resistance and capacitance. Conversely, the diameter of the semicircle for the MXene−graphene electrode is smaller, indicating reduced resistance and capacitance.

The results indicate that the MXene coating could significantly decrease the capacitance of the electrical double layer and improve the conductivity due to its layered structure and metallic nature. During the functionalization steps, resistance and capacitance increased when the surface was functionalized with APTES and immobilized with an antibody. It is important to note that hydrogel encapsulation significantly reduced the resistance and capacitance due to its neutral nature and its role as a barrier to charge transfer, thus successfully suppressing the increase of capacitance caused by the bioprobefunctionalization. Therefore, the combination of MXene and hydrogel reduces the capacitance of the double layer, which in turn increases the shift of the Dirac point, i.e., enhances the sensing signal.[26,36]

4.4. Sensor Fabrication and Functionalization. The bare sensor was fabricated as follows: the poly(dimethylsiloxane) (PDMS) chamber was first bonded to the graphene-covered glass to form the detection chamber. Silver paste was then applied to both sides of the chamber and dried at

https://doi.org/10.1021/acsami.4c12130
ACS Appl. Mater. Interfaces 2025, 17, 2871−2883

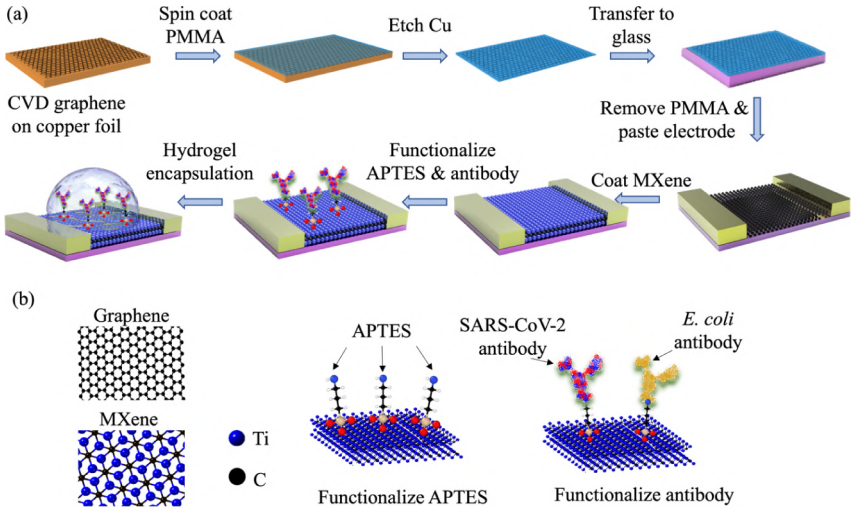


Figure 8. (a) Sensor fabrication and functionalization process; and (b) functionalization details.

50 °C. Subsequently, two wires were soldered to form the sensor's electrodes. Finally, a 50 μL MXene solution was deposited onto the graphene surface and dried in an N_2 environment to avoid oxidation.

In the functionalization process, 50 μL of 25% APTES was first dripped into the chamber. The mixture was then kept for 2 h to ensure the bonding formation between the −OH group on MXene and the $-NH_2$ group on APTES. Next, antibody immobilization was achieved by dripping 20 μL of SARS-CoV-2 antibody or *E. coli* antibody into the chamber, while 50 μL of BSA was applied to avoid nonspecific affinity.

The fabrication and functionalization of the hydrogel-encapsulated sensor (HE sensor) differ from those of the bare sensor in two aspects, as detailed in Figure 8. First, HE sensors do not require the attachment of a PDMS chamber. Second, after BSA treatment, 50 μL of pregel solution is applied to the sensing surface to achieve hydrogel encapsulation. All steps involved in the fabrication and functionalization are summarized in Figure 8.

To confirm the successful functionalization of the MXene−graphene sensing surface, FT-IR was performed to show the chemical group and bonding information. In Figure S6, the peak at around 979 cm^{-1} corresponds to Ti−O−Si, which is formed by the condensation reaction between the OH group on the MXene surface and the NH_2 group of APTES. This demonstrates the successful functionalization of APTES on the sensing surface. Si−O is the representative peak of APTES. The asymmetric and symmetric stretches of $-CH_2$ groups on the alkyl chain at 2963 and 2892 cm^{-1} appeared in the FT-IR spectrum of the APTES-functionalized sample, and the peak at around 3356 cm^{-1} was reduced from the stretching vibration mode of free amine from APTES.[37]

After antibody immobilization, we can see the intensity of NH peaks, especially at around 1595 cm^{-1} deceased, which can be ascribed to the amino groups on APTES forming covalent bonds with the antibody. The BSA curing process shares the same trend as the antibody immobilization process, as it is used for blocking the nonspecific binding and reaction products.[38]

4.5. Selective Transport Experiments. *4.5.1. Hydrogel Preparation.* The pregel solution of the PAAm-hydrogel with *E. coli*-GFP was prepared by dissolving 0.06 g of AAm monomer into 440 μL *E. coli*-GFP solution (with a concentration of approximately 10^6 cells/mL), yielding a final concentration of 12 wt %. The pregel solution of the PAAm-hydrogel with fluorescence-labeled SARS-CoV-2 was prepared by mixing 0.06 g of AAm monomer with 440 μL of diluted fluorescence-labeled SARS-CoV-2 solution (40 μL of fluorescence-labeled SARS-CoV-2 solution diluted in 400 μL of PBS solution). In 500 μL of both pregel solutions, we further added 5.5 μL of 0.1 M APS as the thermal initiator, 25 μL of 0.23 wt % MBAA as the cross-linker, and 1 μL of TEMED as the cross-linking accelerator. Thereafter, the solution was poured into a customized acrylic mold measuring 18 × 18 × 1.5 mm^3 and left to sit for half an hour to complete the hydrogel curing. The mold was covered with aluminum foil to prevent photobleaching. The mesh size ξ of hydrogels can be estimated as 20 nm with $\xi = \sqrt{N}\, b$, where N = 2263 is the ratio of monomer density to cross-linker density and b = 0.43 nm is the size of one AAM monomer.[39]

4.5.2. FRAP Experiment. The experiments were performed on a confocal laser scanning microscope (spectral-based Olympus FluoView) using a 40 × oil immersion objective and a 488 nm laser (10 mW). For the PAAm hydrogel mixed with *E. coli*-GFP, a circular region with a diameter of 20 μm was photobleached for 6 s at full laser power. For the PAAm hydrogel mixed with fluorescence-labeled SARS-CoV-2, a circular region with a diameter of 40 μm was photobleached for 15 s at full laser power.

5. CONCLUSION

In conclusion, we developed a hydrogel-encapsulated MXene−graphene-based FET biosensor that adopts a hydrogel in place of the traditional liquid electrolyte. The mesh-size-designed hydrogel encapsulation functions as a gel-gating and filter, replacing the liquid electrolyte and controlling the diffusion of biomarkers while also serving as an encapsulation layer. The SARS CoV -2 and *E. coli* antibodies were immobilized on the sensing surface to detect SARS-CoV-2 protein and *E. coli* bacteria at different concentrations, demonstrating detection specificity. MD modeling cases were conducted to validate the influence of hydrogels on the electric fields around the surfaces of the sensing materials.

The hydrogel-encapsulated MXene−graphene-based sensor has proven effective in detecting the SARS-CoV-2 biomarker while preventing the diffusion of *E. coli* biomarkers, as their size exceeds that of the hydrogel's mesh openings. Furthermore, the

https://doi.org/10.1021/acsami.4c12130
ACS Appl. Mater. Interfaces 2025, 17, 2871−2883

hydrogel encapsulation enhances the intensity of signal output compared to the bare sensor due to the increased Debye length, which is validated through MD modeling. This design allows for specific detection at ultralow concentrations, achieving SARS-CoV-2 protein detection at 1 fg/mL for both sensors with and without hydrogel encapsulation. Additionally, it enables *E. coli* detection at 7.5×10^{-1} CFU/mL for the sensor without hydrogel encapsulation, while no signal output is observed for the hydrogel-encapsulated sensor due to the selective diffusion effects of the hydrogel.

■ ASSOCIATED CONTENT

Supporting Information

The Supporting Information is available free of charge at https://pubs.acs.org/doi/10.1021/acsami.4c12130.

Video S1: The fluorescence intensity performance of *E. coli*-GFP and fluorescence-labeled SARS-CoV-2 within 2 min following photobleaching (AVI)

Additional details on the time-dependent behavior of SARS-CoV-2 protein detection, XRD and XPS spectra for MXene, EDS results of hydrogel, Nyquist plot measurement for each surface functionalization step, and FT-IR for each surface functionalization step (DOCX)

■ AUTHOR INFORMATION

Corresponding Author

Chenglin Wu − *Zachry Department of Civil and Environmental Engineering, Texas A&M University, College Station, Texas 77843, United States;* orcid.org/0000-0001-7733-1084; Email: chenglinwu@tamu.edu

Authors

Jiaoli Li − *Zachry Department of Civil and Environmental Engineering, Texas A&M University, College Station, Texas 77843, United States*

Jiabin Liu − *Department of Mechanical Engineering, Michigan State University, East Lansing 48824-1312, United States*

Congjie Wei − *Zachry Department of Civil and Environmental Engineering, Texas A&M University, College Station, Texas 77843, United States*

Xinyue Liu − *Department of Mechanical Engineering, Massachusetts Institute of Technology, Cambridge, Massachusetts 02139, United States*

Shaoting Lin − *Department of Mechanical Engineering, Michigan State University, East Lansing 48824-1312, United States*

Complete contact information is available at: https://pubs.acs.org/10.1021/acsami.4c12130

Author Contributions

Conceptualization: C.W., S.L. and X.L.; Experiment: J.L. and J.L.; Modeling: C.W.; Writing—original draft: J.L. and C.W.; Writing—review and editing: all authors; Funding acquisition: C.W. and S.L.

Notes

The authors declare no competing financial interest.

■ ACKNOWLEDGMENTS

This work was supported by the National Science Foundation CMMI#2414719.

■ REFERENCES

(1) Khanmohammadi, A.; Aghaie, A.; Vahedi, E.; Qazvini, A.; Ghanei, M.; Afkhami, A.; Hajian, A.; Bagheri, H. Electrochemical biosensors for the detection of lung cancer biomarkers: A review. *Talanta* **2020**, *206*, 120251.

(2) Patel, S.; Maheshwari, A.; Chandra, A. Biomarkers for wound healing and their evaluation. *J. Wound Care* **2016**, *25* (1), 46−55.

(3) Akolpoglu, M. B.; Bozuyuk, U.; Erkoc, P.; Kizilel, S.. In Biosensing−drug delivery systems for in vivo applications. *In Advanced Biosensors for Health Care Applications*, Elsevier: 2019; 249−262.

(4) Ménard-Moyon, C.; Bianco, A.; Kalantar-Zadeh, K. Two-dimensional material-based biosensors for virus detection. *ACS Sens.* **2020**, *5* (12), 3739−3769.

(5) Castillo-Henríquez, L.; Brenes-Acuña, M.; Castro-Rojas, A.; Cordero-Salmerón, R.; Lopretti-Correa, M.; Vega-Baudrit, J. R. Biosensors for the detection of bacterial and viral clinical pathogens. *J. Sens.* **2020**, *20* (23), 6926.

(6) Kim, J. T.; Choi, H.; Choi, Y.; Cho, J. H. Ion-gel-gated graphene optical modulator with hysteretic behavior. *ACS Appl. Mater. Interfaces* **2018**, *10* (2), 1836−1845.

(7) Yi, H. T.; Rangan, S.; Tang, B.; Frisbie, C. D.; Bartynski, R. A.; Gartstein, Y. N.; Podzorov, V. Electric-field effect on photoluminescence of lead-halide perovskites. *Mater. Today* **2019**, *28*, 31−39.

(8) Yao, B.; Huang, S. W.; Liu, Y.; Vinod, A. K.; Choi, C.; Hoff, M.; Li, Y.; Yu, M.; Feng, Z.; Kwong, D. L.; et al. Gate-tunable frequency combs in graphene−nitride microresonators. *Nature* **2018**, *558* (7710), 410−414.

(9) Wang, Z. L. Piezopotential gated nanowire devices: Piezotronics and piezo-phototronics. *Nano Today* **2010**, *5* (6), 540−552.

(10) Nasrollahzadeh, M.; Sajjadi, M.; Soufi, G. J.; Iravani, S.; Varma, R. S. Nanomaterials and nanotechnology-associated innovations against viral infections with a focus on coronaviruses. *J. Nanomater.* **2020**, *10* (6), 1072.

(11) Li, Y.; Peng, Z.; Holl, N. J.; Hassan, M. R.; Pappas, J. M.; Wei, C.; Izadi, O. H.; Wang, Y.; Dong, X.; Wang, C.; et al. MXene−graphene field-effect transistor sensing of influenza virus and SARS-CoV-2. *ACS Omega* **2021**, *6* (10), 6643−6653.

(12) Dai, X.; Vo, R.; Hsu, H. H.; Deng, P.; Zhang, Y.; Jiang, X. Modularized field-effect transistor biosensors. *Nano Lett.* **2019**, *19* (9), 6658−6664.

(13) Lei, Y. M.; Xiao, M. M.; Li, Y. T.; Xu, L.; Zhang, H.; Zhang, Z. Y.; Zhang, G. J. Detection of heart failure-related biomarker in whole blood with graphene field effect transistor biosensor. *Biosens. Bioelectron.* **2017**, *91*, 1−7.

(14) Wang, S.; Hossain, M. Z.; Shinozuka, K.; Shimizu, N.; Kitada, S.; Suzuki, T.; Ichige, R.; Kuwana, A.; Kobayashi, H. Graphene field-effect transistor biosensor for detection of biotin with ultrahigh sensitivity and specificity. *Biosens. Bioelectron.* **2020**, *165*, 112363.

(15) Béraud, A.; Sauvage, M.; Bazán, C. M.; Tie, M.; Bencherif, A.; Bouilly, D. Graphene field-effect transistors as bioanalytical sensors: Design, operation and performance. *Anal* **2021**, *146* (2), 403−428.

(16) Shen, M. Y.; Li, B. R.; Li, Y. K. Silicon nanowire field-effect-transistor based biosensors: From sensitive to ultra-sensitive. *Biosens. Bioelectron.* **2014**, *60*, 101−111.

(17) Sharma, S.; Moudgil, A.; Singh, S.; Mishra, P.; Das, S. Highly Sensitive,Rapid, and Real-Time Detection of Hydrogen Sulfide in Human Blood Plasma Using $MoSe_2$ Field-Effect Transistor. *IEEE Trans. Electron Devices* **2023**, *70* (1), 275−280.

(18) Liu, C.; Wei, X.; Hao, S.; Zong, B.; Chen, X.; Li, Z.; Mao, S. Label-Free, Fast Response, and Simply Operated Silver Ion Detection with a $Ti_3C_2T_x$ MXene Field-Effect Transistor. *Anal. Chem.* **2021**, *93* (22), 8010−8018.

(19) Hao, S.; Liu, C.; Chen, X.; Zong, B.; Wei, X.; Li, Q.; Qin, H.; Mao, S. $Ti_3C_2T_x$ MXene sensor for rapid Hg2+ analysis in high salinity environment. *J. Hazard. Mater.* **2021**, *418*, 126301.

(20) Chen, X.; Liu, Y.; Fang, X.; Li, Z.; Pu, H.; Chang, J.; Chen, J.; Mao, S. Ultratrace antibiotic sensing using aptamer/graphene-based field-effect transistors. *Biosens. Bioelectron.* **2019**, *126*, 664−671.

(21) Schroter, M.; Claus, M.; Sakalas, P.; Haferlach, M.; Wang, D. Carbon nanotube FET technology for radio-frequency electronics: State-of-the-art overview. *IEEE J. Electron Devices Soc.* **2013**, *1* (1), 9−20.
(22) Bay, H. H.; Vo, R.; Dai, X.; Hsu, H. H.; Mo, Z.; Cao, S.; Li, W.; Omenetto, F. G.; Jiang, X. Hydrogel gate graphene field-effect transistors as multiplexed biosensors. *Nano Lett.* **2019**, *19* (4), 2620−2626.
(23) Olvera, D.; Monaghan, M. G. Electroactive material-based biosensors for detection and drug delivery. *Adv. Drug Delivery Rev.* **2021**, *170*, 396−424.
(24) Varshney, P. K.; Gupta, S. Natural polymer-based electrolytes for electrochemical devices: a review. *Ionics* **2011**, *17* (6), 479−483.
(25) Dumitru, L. M.; Manoli, K.; Magliulo, M.; Ligonzo, T.; Palazzo, G.; Torsi, L. A hydrogel capsule as gate dielectric in flexible organic field-effect transistors. *APL Mater.* **2015**, *3* (1), 014904.
(26) Li, Y.; Peng, Z.; Li, J.; Wei, C.; Liu, S.; Hao, W.; Cheng, H.; Burton, C.; Wang, Y.; Huang, Y. W.; Kim, C.-S.; et al. Wearable MXene-Graphene Sensing of Influenza and SARS-CoV-2 Virus in Air and Breath: From Lab to Clinic. *Adv. Mater. Technol.* **2024**, *9* (3), 2201787.
(27) Erickson, H. P. Size and shape of protein molecules at the nanometer level determined by sedimentation, gel filtration, and electron microscopy. *Biol. Proced Online* **2009**, *11*, 32−51.
(28) Soumpasis, D. Theoretical analysis of fluorescence photobleaching recovery experiments. *Biophys. J.* **1983**, *41* (1), 95−97.
(29) Lin, S.; Londono, C. D.; Zheng, D.; Zhao, X. An extreme toughening mechanism for soft materials. *J. Soft Matter* **2022**, *18* (31), 5742−5749.
(30) Zhao, S.; Surwade, S. P.; Li, Z.; Liu, H. Photochemical oxidation of CVD-grown single layer graphene. *J. Nanotechnol.* **2012**, *23* (35), 355703.
(31) Wall, M. The Raman spectroscopy of graphene and the determination of layer thickness. *J. Therm. Sci.* **2011**, *5*, 1−5.
(32) Chen, T.; Tong, G.; Xu, E.; Li, H.; Li, P.; Zhu, Z.; Tang, J.; Qi, Y.; Jiang, Y. Accelerating hole extraction by inserting 2D Ti_3C_2-MXene interlayer to all inorganic perovskite solar cells with long-term stability. *J. Mater. Chem. A* **2019**, *7* (36), 20597−20603.
(33) Cao, Y.; Deng, Q.; Liu, Z.; Shen, D.; Wang, T.; Huang, Q.; Du, S.; Jiang, N.; Lin, C. T.; Yu, J. Enhanced thermal properties of poly (vinylidene fluoride) composites with ultrathin nanosheets of MXene. *RSC Adv.* **2017**, *7* (33), 20494−20501.
(34) Aziz, S. B.; Dannoun, E. M.; Murad, A. R.; Mahmoud, K. H.; Brza, M. A.; Nofal, M. M.; Elsayed, K. A.; Abdullah, S. N.; Hadi, J. M.; Kadir, M. F. Influence of scan rate on CV Pattern: Electrical and electrochemical properties of plasticized Methylcellulose: Dextran (MC: Dex) proton conducting polymer electrolytes. *Alex. Eng. J.* **2022**, *61* (8), 5919−5937.
(35) Jash, P.; Parashar, R. K.; Fontanesi, C.; Mondal, P. C. The importance of electrical impedance spectroscopy and equivalent circuit analysis on nanoscale molecular electronic devices. *Adv. Funct. Mater.* **2022**, *32* (10), 2109956.
(36) Hwang, M. T.; Heiranian, M.; Kim, Y.; You, S.; Leem, J.; Taqieddin, A.; Faramarzi, V.; Jing, Y.; Park, I.; van der Zande Am; Van Der Zande, A. M.; Nam, S.; et al. Ultrasensitive detection of nucleic acids using deformed graphene channel field effect biosensors. *Nat. Commun.* **2020**, *11* (1), 1543.
(37) Ji, J.; Zhao, L.; Shen, Y.; Liu, S.; Zhang, Y. Covalent stabilization and functionalization of MXene via silylation reactions with improved surface properties. *FlatChem* **2019**, *17*, 100128.
(38) Vashist, S. K.; Schneider, E. M.; Luong, J. H. Rapid sandwich ELISA-based in vitro diagnostic procedure for the highly-sensitive detection of human fetuin A. *Biosens. Bioelectron.* **2015**, *67*, 73−78.
(39) Tang, J.; Li, J.; Vlassak, J. J.; Suo, Z. Fatigue fracture of hydrogels. *Extreme Mech. Lett.* **2017**, *10*, 24−31.

https://doi.org/10.1021/acsami.4c12130
ACS Appl. Mater. Interfaces 2025, 17, 2871−2883